# The Influence of Anion Composition on Subgap Density of States and Electrical Characteristics in ZnON Thin-Film Transistors

Jun Tae Jang, Hara Kang, Hye Ri Yu, Eok Su Kim, Kyoung Seok Son, Seong-Ho Cho, Dong Myong Kim, *Member, IEEE*, Sung-Jin Choi, and Dae Hwan Kim, *Senior Member, IEEE*

***Abstract*— The influence of anion composition on the electrical characteristics of amorphous zinc-oxynitride thin-film transitors (TFTs) is investigated and quantitatively modeled, with emphasis on the subgap density of states (DOS). As the ratio of N to (N + O) increases, the density of valence band tail states increases, followed by narrowing of the bandgap and a decrease in the density of conduction band tail states, which in turn is followed by either a higher field-effect mobility or a better subthreshold swing; each of these effects is explained. Furthermore, the anion composition dependence of the transconductance degradation at a high bias is analyzed on the basis of the proposed model. In addition, the effects of the N/(N + O) ratio on carrier density and field-effect mobility are quantitatively explained by the ionized nitrogen vacancy ($V_N^{1,3+}$) model observed in shallow donor peak in the DOS and by the charge-controlled mobility model, respectively. Finally, the effect of nanocrystalline structure mixed with amorphous on transport properties is discussed.**

***Index Terms*— Anion composition, ZnON, subgap density of states, thin-film transistors.**

## I. Introduction

RECENTLY, amorphous In–Ga–Zn–O (a-IGZO), which exhibits enhanced mobility compared to ZnO because it contains highly electronegative metal ions ($Ga^{3+}$) and low-ionization-energy ions ($In^{3+}$), which suppress the formation of crystalline grains and potential barriers in ZnO, has been successfully introduced as the channel layer of thin-film transistors (TFTs) for commercial applications such as ultra-high-definition and large-area displays [1]. However, the mobility of a-IGZO TFTs, which have become a mature technology as result of the co-design of performance, stability, and cost, is limited to less than 10 cm $^2$ V$^{-1}$ s$^{-1}$ [1], which is insufficient for driving next-generation displays and sensors. In amorphous multi-metal oxides, some potential barriers between neighboring ions inherently exist; these barriers hinder electron transport and lower the mobility because of the different radii of metal ions, which results in non-uniform overlap of conduction electron orbitals. Thus, the anion-controlled ZnO− i.e., zincoxynitride (ZnON), whose mobility is greater than that of a-IGZO because N ions affect only the valence band and because single-metal $Zn^{2+}$ ions can suppress the formation of potential barriers in the conduction band- has been proposed and successfully demonstrated; its field-effect mobility exceeds 50 cm $^2$ V$^{-1}$ s$^{-1}$ [2]–[4] and is stable under illumination [5], [6].

The systematic control of anions is indispensable for realizing ZnON TFTs with performance comparable with that of a-IGZO TFTs. To this point, the anion control of ZnON has not been investigated from the viewpoint of the electrical characteristics of TFTs but rather from the perspective of thin-film bulk; thus, previous analyses have focused on either the competition between the crystallinity and non-crystallinity [7] or the competitive growth reactions that occur during the formation of ZnO and $Zn_3$ $N_2$ materials [8]. Even in the extremely small number of ZnON TFT studies on the influence of anion content on the trap density [9], the anion composition-dependent trap distribution in the subgap energy, i.e., the subgap density of states (DOS) $g(E)$, has rarely been investigated [10], although control of the anions plays a critical role in optimizing the complicated trade-off between the performance and stability of ZnON TFTs [5].

In this work, we investigate the effects of anion composition on the subgap DOS and on the electrical characteristics of ZnON TFTs and quantitatively model these effects by extracting the DOS from the photoresponse component of the TFT capacitance–voltage ($C - V$) characteristics. We control the anion composition by modulating the flow rate of reactant gas during the sputtered deposition of the active layer. The nitrogen vacancy ($V_N$)-related shallow donor peak is clearly observed for the first time in the energy level 0.15 eV below the conduction band minimum ($E_C$). Furthermore, key TFT characteristics such as the source/drain (S/D) series resistance-induced transconductance ($g_m$) degradation, charge-controlled mobility, and carrier concentration are explained consistently using the extracted DOS and the proposed model.

## II. Experiments

The ZnON TFTs with an inverted staggered bottom-gate and top-contact configuration were fabricated on glass

Manuscript received November 14, 2018; accepted November 22, 2018. Date of publication November 28, 2018; date of current version January 9, 2019. This work was supported in part by the National Research Foundation of Korea funded by the South Korean Government (MSIP) under Grant 2016R1A5A1012966, in part by the Ministry of Education, Science and Technology under Grant 2017R1A2B4006982, in part by SILVACO, for providing the CAD software, and in part by the IC Design Education Center. The review of this letter was arranged by Editor S.-J. Chang. *(Jun Tae Jang and Hara Kang contributed equally to this work.) (Corresponding author: Dae Hwan Kim.)*

J. T. Jang, H. Kang, H. R. Yu, D. M. Kim, S.-J. Choi, and D. H. Kim are with the School of Electrical Engineering, Kookmin University, Seoul 136-702, South Korea (e-mail: drlife@kookmin.ac.kr).

E. S. Kim, K. S. Son, and S.-H. Cho are with the Samsung Advanced Institute of Technology, Suwon 448-803, South Korea.

Color versions of one or more of the figures in this letter are available online at http://ieeexplore.ieee.org.

Digital Object Identifier 10.1109/LED.2018.2883732

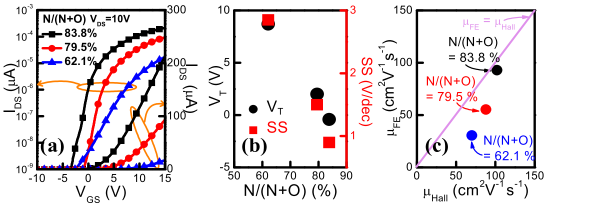


Fig. 1. The N/(N+O) ratio-dependences of (a) transfer characteristics, (b) $V_T$ and SS, and (c) $\mu_{FE}$ and $\mu_{Hall}$.

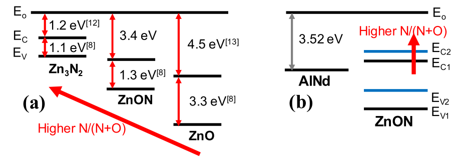


Fig. 2. Schematics illustrating the N/(N+O) ratio-dependences of (a) the ZnON compared with $Zn_3N_2$ and ZnO and (b) the $\phi_{SB}$ between ZnON and AlNd S/D electrodes.

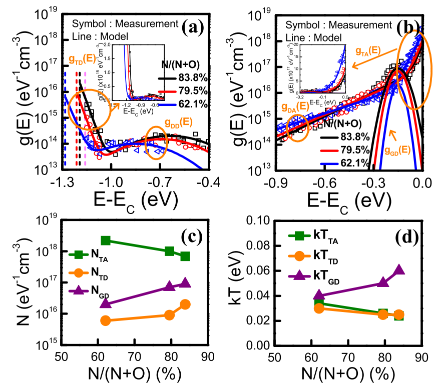


Fig. 3. Experimentally extracted subgap DOS profile near (a) the $E_V$ and (b) $E_C$. The N/(N+O) ratio-dependences of (c) densities and (d) characteristic energies of the subgap DOS.

TABLE I

MODEL EQUATIONS AND PARAMETERS OF THE SUBGAP DOS

| Parameter N/(N+O) | Value 83.8 % | 79.5 % | 62.1 % | Unit |
|---|---|---|---|---|
| Acceptor-like DOS | $g_{TA}(E)+g_{DA}(E)=N_{TA}\times\exp\left(-\frac{E_C-E}{kT_{TA}}\right)+N_{DA}\times\exp\left(-\frac{E_C-E}{kT_{DA}}\right)$ | | | |
| $N_{TA}/kT_{TA}$ | $6.9\times10^{17}/0.024$ | $1.0\times10^{18}/0.026$ | $2.2\times10^{18}/0.034$ | $eV^{-1}cm^{-3}/eV$ |
| $N_{DA}/kT_{DA}$ | $9.0\times10^{16}/0.14$ | $6.8\times10^{16}/0.155$ | $2.8\times10^{16}/0.21$ | $eV^{-1}cm^{-3}/eV$ |
| Donor-like DOS | $g_{TD}(E)+g_{DD}(E)+g_{GD}(E)=N_{TD}\times\exp\left(-\frac{E-E_V}{kT_{TD}}\right)+N_{DD}\times\exp\left(-\left(\frac{E-E_V-E_{DD}}{kT_{DD}}\right)^2\right)+N_{GD}\times\exp\left(-\left(\frac{E-E_V-E_{GD}}{kT_{GD}}\right)^2\right)$ | | | |
| $N_{TD}/kT_{TD}$ | $2.0\times10^{16}/0.025$ | $9.0\times10^{15}/0.025$ | $6.0\times10^{15}/0.03$ | $eV^{-1}cm^{-3}/eV$ |
| $N_{DD}/kT_{DD}/E_{DD}$ | $2.0\times10^{14}/0.28/0.55$ | $1.5\times10^{14}/0.27/0.52$ | $1.0\times10^{14}/0.27/0.43$ | $eV^{-1}cm^{-3}/eV/eV$ |
| $N_{GD}/kT_{GD}/E_{GD}$ | $9.0\times10^{16}/0.06/0.15$ | $7.0\times10^{16}/0.05/0.15$ | $2.0\times10^{16}/0.04/0.15$ | $eV^{-1}cm^{-3}/eV/eV$ |

substrates using a standard semiconductor fabrication process. TFT device integration was performed by first depositing a 200-nm-thick Mo gate by direct-current (DC) sputtering at room temperature. A dielectric stack of 350-nm-thick $SiN_x$ and 50-nm-thick $SiO_x$ were then deposited at 350 °C by plasma-enhanced chemical vapor deposition (PECVD). The ZnON active layer with a thickness of 50 nm was subsequently deposited through a reactive radio-frequency magnetron sputtering process using a Zn target with $N_2$ and $O_2$ gas as reactants and was patterned by wet etching. To control the anion composition, the $O_2$ gas flow rate was modulated as 2, 3, and 4 sccm while the $N_2$ (100 sccm) and Ar (10 sccm) flow rates were kept constant, which was found to correspond to N/(N+O) nitrogen anion ratios of 83.8, 79.5, and 62.1 % respectively from Rutherford backscattering spectrometry analysis. Subsequently, a 100-nm-thick $SiO_2$ etch-stopper layer was deposited at 200 °C by PECVD and was patterned by dry etching. Then, AlNd was deposited by DC sputtering and patterned by dry etching to form the source-drain electrodes, which formed non-negligible S/D series resistance ($R_{SD}$) owing to Schottky barrier between the ZnON active film and AlNd S/D electrodes. The $SiO_2$ passivation layer was additionally formed on the $SiO_2$ etch-stopper layer of the ZnON TFTs. Finally, TFT devices were annealed in air at 250 °C for 1 hr. The ZnON films were confirmed from a grazing incidence angle X-ray diffraction to retain the amorphous-like structure with a smooth surface topography with a small root mean square surface roughness of 0.7 nm and may contain the nanocrystalline structure in part [8].

The ZnON TFT device with channel width/length ($W/L$) = 50/50 $\mu$m/$\mu$m was characterized at room temperature, in darkness, and under ambient atmosphere using an Agilent 4156C precision parameter analyzer. The $C$–$V$ data were collected at a frequency of 50 kHz using an HP 4284A precision LCR meter. The subgap DOS, $g(E)$, was extracted from the photo-response of $C$–$V$ characteristics with a wavelength of 1064 nm and an optical power of 2 mW [11].

## III. RESULTS AND DISCUSSION

The electrical parameters of the fabricated ZnON TFT are shown in Fig. 1. The threshold voltage ($V_T$) and subthreshold swing (SS) increase and the field-effect mobility ($\mu_{FE}$) decreases with decreasing N/O ratio equivalently with the increase of oxygen, where $\mu_{FE}$ is extracted in $V_{GS} - V_T = V_{DS} = 10$ V. The N/O ratio-dependences of $V_T$, SS, and $\mu_{FE}$ will be discussed later including the comparison between $\mu_{FE}$ and Hall mobility ($\mu_{Hall}$) which is measured from ZnON thin-film bulk.

Electron affinities and bandgap energies of $Zn_3N_2$, ZnON, and ZnO are as seen in Fig. 2(a) [8], [12], [13], where $E_0$, $E_C$, and $E_V$ are the vacuum level, conduction band minimum level, and valence band maximum level, respectively. As the N/(N+O) ratio increases, the electron affinity as well as the bandgap energy of ZnON decreases because the active thin-film is dominated by $Zn_3N_2$ rather than by ZnO against the competition between reactions for the growth of cubic $Zn_3N_2$ and for growth of hexagonal ZnO in a reactive sputtering process. Consistently, the N/(N+O)-dependent bandgap energy was found to be 1.20 (N/(N+O) = 0.838), 1.21 (0.795), and 1.27 eV (0.621), which was measured from visible-IR spectrometer analysis. The increase of N/O ratio would also increase the height of Schottky barrier ($\phi_{SB}$) between ZnON and S/D electrodes, which possibly increases $R_{SD}$ as seen in Fig. 2(b).

Figure 3 shows the extracted subgap DOS. The subgap DOS, model equations, and parameters are summarized in Table I. With increasing N/O ratio, an increase in the valence band tail (VBT) states, i.e., $g_{TD}(E)$, followed by bandgap narrowing is observed, as shown in Fig. 3(a), 3(c), 3(d) and Table I. The bandgap narrowing with increasing N/(N+O) ratio is explained as follows. The VBT states are introduced by

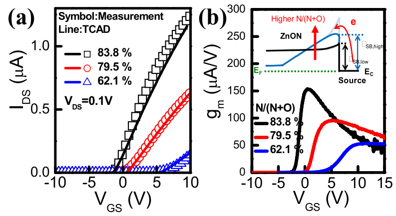


Fig. 4. (a) The transfer characteristics (symbol is the measurement and line is the TCAD simulation). (b) The measured transconductance characteristics (inset: the N/(N+O) ratio-dependence of the $\phi_{SB}$).

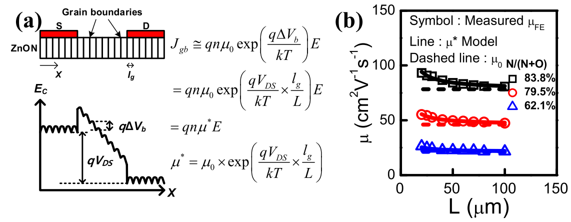


Fig. 5. (a) Schematic illustration and $\mu^*$ model equation considering the ZnON nanocrystalline structure. (b) Comparison between the measured $L$-dependent $\mu_{FE}$ and $\mu^*$ model. Dashed lines indicate $\mu_0$.

the hybridization of N $2p$ and O $2p$ orbitals [5]. Thus, as seen in Fig. 3(a), the $g_{TD}(E)$ and $g_{DD}(E)$ increase with increasing N ratio because of the increase in N $2p$ orbitals. The N $2p$ band located above the oxygen $2p$ band becomes occupied because of the high N content; accordingly, the $E_V$ level is elevated above the level of oxygen vacancy ($V_O$)-related deep-level defects, which results in both the narrowing of the bandgap and the suppression of persistent photoconductivity (PPC) [5].

However, the localized states near the $E_C$ ($g_{TA}$ and $g_{DA}$) decrease with increasing N/(N+O) ratio as observed in Fig. 3(b)–(d), and Table I. Interestingly, the shallow donor defect $g_{GD}$ which is related with $V_N$ [10] is clearly observed for the first time in the energy level of 0.15 eV below the $E_C$, which decreases with the addition of oxygen and becomes negligible in the case of N/(N+O) = 0.621. These results suggest that the crystallinity of ZnON strongly depends on the oxygen content.

The $g_{TA}$ well explains the dependences of $V_T$, SS, and $\mu_{FE}$ on the N/(N+O) ratio. The $N_{TA}$ increases with decreasing N/(N+AO) ratio, which results in an increase in the $V_T$ and the SS and in a decrease of the $\mu_{FE}$. While a higher $\mu_{FE}$ of ZnON TFTs with increasing N ratio can be explained mainly by the low effective mass of $Zn_3$ $N_2$ [5], our results show that the $N_{TA}$ is a good indicator for the $\mu_{FE}$ as well as for the $V_T$ and the SS. Consistently, the electron density and the on-current decrease upon the addition of oxygen (decreased $V_N$), as evident in Fig. 1(a). In addition, $\mu_{Hall}$ is compared with $\mu_{FE}$ as shown in Fig. 1(c). While $\mu_{FE}$ is nearly the same with $\mu_{Hall}$ in the case of N/(N+O) = 83.8%, $\mu_{FE}$ becomes much lower than $\mu_{Hall}$ as the N/(N+O) ratio decreases. This phenomenon is explained as follows. $\mu_{Hall}$ is measured in the ZnON thin-film bulk and $\mu_{FE}$ is extracted from TFT characteristic. Then, $\mu_{FE}$ is typically lower than $\mu_{Hall}$ because of the surface scattering resulting from the TFT process-induced traps. Therefore, as the N/(N+O) ratio decreases, the conduction band tail trap density increases [higher $g_{TA}$ in Fig. 3] and the difference between $\mu_{Hall}$ and $\mu_{FE}$ increases [Fig. 1(c)].

For a quantitative validation, we incorporated our DOS model into a TCAD simulator [14]. The used conduction band mobility $\mu_{Band}$ was calculated using the equation $\mu_{FE} \times (Q_{free} + Q_{loc})/Q_{free}$, where $Q_{free}$ is the free charge density, and $Q_{loc}$ is the localized charge density from the DOS. Figure 4(a) shows that the simulated $I - V$ curves agree well with the measured ones when the carrier doping density $N$ is $1.3 \times \int g_{GD}dE$ over a subgap energy range, which suggests that the shallow donor effects of $V_N^{+}$, $V_N^{2+}$, and $V_N^{3+}$ [15] can be effectively modeled as $V_N^{1.3+}$. In addition, the N/(N+O) effect on the $R_{SD}$-induced $g_m$ degradation at a high $V_{GS}$ was examined, as shown in Fig. 4(b). The $g_m$ degradation was mitigated by the addition of oxygen because of the increase of electron affinity, which was accompanied by lowering of $\phi_{SB}$ between the S/D electrode and active film, i.e., by a lower $R_{SD}$ with decreasing N/(N+O) ratio, as illustrated in Fig. 2(b) and in the inset of Fig. 4(b).

Finally, to evaluate the effect of nanocrystal on transport properties, the transport model in [16] which combines the drift-diffusion and thermionic emission through grain boundaries was used as follows, $\mu^* = \mu_0 \times \exp(qV_{DS}/kT) \times \exp(l_g/L)$, where $q$, $l_g$, $\mu_0$, $kT$, and $\mu^*$ are the electron charge, grain size, mobility without grain, thermal energy and effective mobility with grain, respectively. Then, we can extract the average $l_g$ through the $L$-dependence of $\mu_{FE}$. The measured $L$-dependent $\mu_{FE}$ (symbol) agrees well with the $\mu^*$ model (line) as shown in Fig. 5. By fitting the measured $\mu_{FE}$ with $\mu^*$ model, the calculated results show that the $l_g$ is approximately 9.6 nm. For more quantitative analysis, the nanocrystallinity factor $\eta$ was defined as $\eta = (\mu^* - \mu_0)/\mu_0$, which means the degree to which $\mu^*$ deviates from the amorphous-dominant value, i.e., $\mu_0$, due to the effect of nanocrystal structure. Then, $\eta$ was extracted to be 7.7%, which means the nanocrystal nature is evaluated to be less than 10% in our ZnON TFTs. Therefore, it was found that the atomic structure of our ZnON TFT is close to an amorphous-dominant structure at least in perspective of transport properties.

## IV. Conclusions

We quantitatively investigated the effect of anion composition, i.e., the ratio of N/(N+O), on the subgap DOS and the electrical characteristics of amorphous ZnON TFTs. The $V_N$ shallow donor peak $g_{GD}$ was clearly observed at 0.15 eV below the $E_C$ and was well correlated with the carrier density via the $V_N^{1.3+}$ model. We also observed that the $\mu_{FE}$ is successfully described by the charge-controlled model, i.e., $\mu_{FE} = \mu_{Band} \times Q_{free} / (Q_{free} + Q_{loc})$ combine with DOS. With increasing N/(N+O) ratio, the higher $g_{TD}$ and broader $g_{DD}$ result in bandgap narrowing and the $g_m$ degradation at a high $V_{GS}$ becomes more significant because of the decrease of electron affinity followed by a higher $\phi_{SB}$ and $R_{SD}$ increase. Furthermore, the $g_{TA}$ well explains the anion composition dependences of the $\mu_{FE}$, $V_T$, SS, and gap between $\mu_{FE}$ and $\mu_{Hall}$. We expect our results to provide a potentially useful tool for the consolidated design and optimization of ZnON materials, processes, and devices.

## REFERENCES


[1] N. Gong, C. Park, J. Lee, I. Jeong, H. Han, J. Hwang, J. Park, K. Park, H. Jeong, Y. Ha, and Y. Hwang, "Implementation of 240 Hz 55-inch ultra definition LCD driven by a-IGZO semiconductor TFT with copper signal lines," in *SID Symp. Dig. Tech. Papers*, vol. 43, no. 1, Jun. 2012, pp. 784–787, doi: 10.1002/j.2168-0159.2012.tb05902.x.

[2] K.-C. Ok, H.-K. Jeong, H.-S. Kim, and J.-S. Park, "Highly stable ZnON thin-film transistors with high field-effect mobility exceeding 50cm$^2$/Vs," *IEEE Electron Device Lett.*, vol. 36, no. 1, pp. 38–40, Jan. 2015, doi: 10.1109/LED.2014.2365614.

[3] C. I. Kuan, H. C. Lin, P. W. Li, and T. Y. Huang, "High-performance submicrometer ZnON thin-film transistors with record field-effect mobility," *IEEE Electron Device Lett.*, vol. 37, no. 3, pp. 303–305, Mar. 2016, doi: 10.1109/LED.2016.2518404.

[4] J. Park, Y. S. Kim, J. H. Kim, K. Park, Y. C. Park, and H.-S. Kim, "The effects of active layer thickness and annealing conditions on the electrical performance of ZnON thin-film transistors," *J. Alloys Compounds*, vol. 688, pp. 666–671, Dec. 2016, doi: 10.1016/j.jallcom.2016.07.245.

[5] H.-S. Kim, S. H. Jeon, J. S. Park, T. S. Kim, K. S. Son, J.-B. Seon, S.-J. Seo, S.-J. Kim, E. Lee, J. G. Chung, H. Lee, S. Han, M. Ryu, S. Y. Lee, and K. Kim, "Anion control as a strategy to achieve high-mobility and high-stability oxide thin-film transistors," *Sci. Rep.*, vol. 3, Mar. 2013, Art. no. 1459, doi: 145910.1038/srep01459.

[6] J.-T. Jang, J. Park, B. D. Ahn, D. M. Kim, S.-J. Choi, H.-S. Kim, and D. H. Kim, "Study on the photoresponse of amorphous In–Ga–Zn–O and zinc oxynitride semiconductor devices by the extraction of sub-gap-state distribution and device simulation," *ACS Appl. Mater. Interfaces*, vol. 7, no. 28, pp. 15570–15577, Jun. 2015, doi: 10.1021/acsami.5b04152.

[7] Y. Ye, R. Lim, and J. M. White, "High mobility amorphous zinc oxynitride semiconductor material for thin film transistors," *J. Appl. Phys*, vol. 106, no. 7, pp. 0745512-1–0745512-8, Oct. 2009, doi: 10.1063/1.3236663.

[8] E. Lee, A. Benayad, T. Shin, H. Lee, D.-S. Ko, T. S. Kim, K. S. Son, M. Ryu, S. Jeon, and G.-S. Park, "Nanocrystalline ZnON; High mobility and low band gap semiconductor material for high performance switch transistor and image sensor application," *Sci. Rep.*, vol. 4, May 2014, Art. no. 4948, doi: 10.1038/srep04948.

[9] F. Xian, J. Ye, S. Gu, H. H. Tan, and C. Jagadish, "Structural transition, subgap states, and carrier transport in anion-engineered zinc oxynitride nanocrystalline films," *Appl. Phys. Lett.*, vol. 109, no. 2, pp. 023109-1–023109-5, Jul. 2016, doi: 10.1063/1.4958294.

[10] T. S. Kim, H.-S. Kim, J. S. Park, K. S. Son, E. S. Kim, J.-B. Seon, S. Lee, S.-J. Seo, S.-J. Kim, S. Jun, K. M. Lee, D. J. Shin, J. Lee, C. Jo, S.-J. Choi, D. M. Kim, D. H. Kim, M. Ryu, S.-H. Cho, and Y. Park, "High performance gallium-zinc oxynitride thin film transistors for next-generation display applications," in *IEDM Tech. Dig.*, Dec. 2013, pp. 27.1.1–27.1.3, doi: 10.1109/IEDM.2013.6724701.

[11] H. Bae, H. Choi, S. Jun, C. Jo, Y. H. Kim, J. S. Hwang, J. Ahn, S. Oh, J.-U. Bae, S.-J. Choi, D. H. Kim, and D. M. Kim, "Single-scan monochromatic photonic capacitance-voltage technique for extraction of subgap DOS over the bandgap in amorphous semiconductor TFTs," *IEEE Electron Device Lett.*, vol. 34, no. 12, pp. 1524–1526, Dec. 2013, doi: 10.1109/LED.2013.2287511.

[12] Z. Wu, "Electronic structures of 3d-metal mononitrides," *J. Comput. Chem.*, vol. 27, no. 3, pp. 267–276, Feb. 2006, doi: 10.1002/jcc.20314.

[13] K. Jacobi, G. Zwicker, and A. Gutmann, "Work function, electron affinity and band bending of zinc oxide surfaces," *Surf. Sci.*, vol. 141, pp. 109–125, Jun. 1984, doi: 10.1016/0039-6028(84)90199-7.

[14] *ATLAS User's Manual*, Silvaco, Santa Clara, CA, USA, 2016.

[15] S. Lee, A. Nathan, Y. Ye, Y. Guo, and J. Robertson, "Localized tail states and electron mobility in amorphous ZnON thin film transistors," *Sci. Rep.*, vol. 5, pp. 13467-1–13467-9, Aug. 2015, doi: 10.1038/srep13467.

[16] F. M. Hossain, J. Nishii, S. Takagi, A. Ohtomo, T. Fukumura, H. Fujioka, H. Ohno, H. Koinuma, and M. Kawasaki, "Modeling and simulation of polycrystalline ZnO thin-film transistors," *J. Appl. Phys.*, vol. 94, no. 12, p. 7768, Aug. 2003, doi: 10.1063/1.1628834.